Conference on Modelling Fluid Flow (CMFF'22)
The 18th International Conference on Fluid Flow Technologies
Budapest, Hungary, August 30-September 2, 2022

Mushroom shaped bubbles and the jet of 1000 m/s

Max KOCH[1], Christiane LECHNER[2,3], Werner LAUTERBORN[2], Robert METTIN[2]

[1] Corresponding Author. Third Physical Institute, Georg-August University Göttingen. Friedrich-Hund-Platz 1, 37077 Göttingen, Germany. E-mail: max.koch@phys.uni-goettingen.de
[2] Third Physical Institute, Georg-August University Göttingen. Friedrich-Hund-Platz 1, 37077 Göttingen, Germany.
[3] Institute of Fluid Mechanics and Heat Transfer, TU Wien, Getreidemarkt 9, 1060 Vienna, Austria

ABSTRACT

The dynamics of a single, laser-induced cavitation bubble on top of a solid cylinder is studied both experimentally and numerically. When the bubble is generated close to the flat top along the axis of the cylinder and its maximum radius exceeds the one of the flat top surface, it collapses in the form of a mushroom with a footing on the cylinder, a long stem and a hat-like cap typical for a mushroom head. The head may collapse forming a thin, fast liquid jet into the stem, depending on bubble size and bubble distance to the top of the cylinder. The parameter space of initial distance to the cylinder, bubble size and cylinder radius is scanned numerically, partly compared to experiments and evaluated for the resulting jet velocity and jet length and other features. The results represent a contribution to understand the behavior of bubbles collapsing close to structured surfaces, in particular, how thin, fast jets are generated. An indication how the fast jet plays a role for erosion is given, as well.

Keywords: single cavitation bubble, CFD, high-speed imaging, laser-induced, rigid cylinder, fast jet

NOMENCLATURE

D	$[m]$	distance bubble – object
R	$[m]$	bubble radius
p	$[Pa]$	pressure
$\boldsymbol{U}$	$[m/s]$	velocity
α	$[-]$	phase parameter
λ	$[m]$	wavelength
μ	$[Pa\,s]$	viscosity
ρ	$[kg/m^3]$	density

Subscripts and Superscripts

max	maximum
eq	equivalent
init	initial
*	normalized quantity
n,∞	quantity at normal conditions

1. INTRODUCTION

The phenomena described in this manuscript are explained in detail in [1]. This manuscript is to be understood as a summary of the main aspects from this publication, plus a small extension. For a full comprehension it is advisable to read the open access article [1] as well. The present manuscript is written with the assumption of familiarity of the reader with the single bubble cavitation phenomenon. If a text part in this manuscript is cited directly from [1] it is denoted by "([1])" at the end of the paragraph.

Despite considerable efforts to elucidate the erosion process by cavitation bubbles, the precise mechanisms are still under discussion. The dynamics of the bubble is highly influenced by many factors: The properties of the surrounding liquid (density, viscosity), the bubble contents (gas, vapour), the bubble–liquid interface (surface tension, coating), outer factors (pressure, temperature, gravity) and, in particular, the large class of geometrical constraints, i.e., boundaries or objects nearby with different properties from flat to curved or smooth to corrugated and solid to soft. For systematic studies on geometrical constraints, isolated single bubbles are required. The liquid breakdown induced by a focused laser light pulse has been used for this purpose ([1]).

In the past, investigation of bubble dynamics near structured objects got less attention than studies on flat or smooth surfaces. However, it is known that cavitation bubbles can reach, clean and also damage crevices, holes, trenches and other complicated surface features (see, e.g., [2]). Up to now, owing to the large variety of structures and constraints, only a few cases were already investigated for single bubble dynamics. Among the solid boundaries and objects, there are a small hole [3], blind holes/crevices [4], rectangular channels [5], convex surfaces [6], a thin gap (parallel plates) [7, 8], rigid spheres [9, 10], a pencil-like electrode [11], ridges and grooves [12], a micro structured riblet [13], edges [14, 15] and corners [16]. ([1]).

The investigation of the dynamics of a bubble close to the top of a rigid cylinder, both experimental and numerical, is described in this manuscript. The bubble is generated on the symmetry axis of the cylinder. Therefore, three independent parameters describe the geometrical arrangement as shown in Figure 1: l_p — the length of the cylinder (height above a planar, solid boundary), r_p — the radius of the cylinder and D_{init} — the distance of the bubble to the top of the cylinder at $t = 0$ (i.e. the spot of optical breakdown, hence the plasma spot). The energy of the bubble, given a certain atmospheric pressure, is classified by the maximum radius $R_{max,unbound}$ the bubble would attain in an unbounded liquid. When the bubble is generated close to an object, the maximum, volume-equivalent radius $R_{max,eq}$ will differ from the unbounded one, depending on the structure of the object and D_{init} (see also [17]).

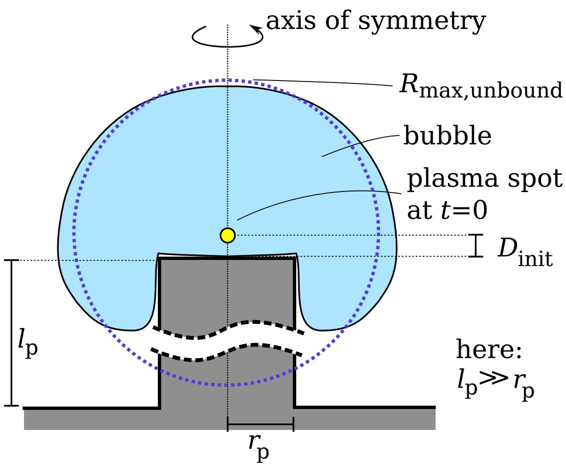

Figure 1. Sketch of the parameters for classification of bubbles close to a solid cylinder [1].

The dynamics of the bubble scale with the non-dimensionalized parameters

$$D^* = \frac{D_{init}}{R_{max,unbound}}, \quad r_p^* = \frac{r_p}{R_{max,unbound}}, \tag{1}$$

for $l_p \gg r_p$. With the reference to $R_{max,unbound}$, the temporal normalization is uniquely defined by the Rayleigh collapse time t_{Rc} given by

$$t_{Rc} = 0.91468 \cdot R_{max,unbound} \sqrt{\rho_\infty / p_\infty}, \tag{2}$$

where $\rho_\infty = 998.2\,kg/m^3$ and $p_\infty = 101315\,Pa$. ([1]).

The case where $l_p = 0$ or $r_p \to \infty$ was and still is heavily studied, it is the case of a bubble close to a flat, rigid boundary. In this case, the bubble will involute and produce a liquid jet towards the solid. Historically, values for $D^* > 0.3$ were investigated, where the jet is called *micro-jet* and exhibits speeds in the order of $100\,m/s$.

Recently, the work by Lechner et al. [18, 19] predicted and described in detail that for $D^* \leq 0.2$, $l_p = 0$ the jet speeds are of one order of magnitude higher. In this parameter subspace, a different jetting mechanism occurs, producing the *fast jet*. The fast jets reach speeds in the order of $1000\,m/s$. They are produced by annular inflow with self-impact and by squeezing the liquid into two opposite directions [20]. The findings are in agreement with the simulations by Pishchalnikov et al. [21] and experiments as early as by Benjamin and Ellis [22]. A comparison with very good agreement of the velocities of numerical simulations with experiments of laser-induced bubbles for both the micro-jet and for the fast jet, as well, can be found in the works of Koch [23] and Koch et al. [24]. Later, these results were confirmed by Reuter et al. [25].

Thus, the question arises, whether there are other geometrical configurations where the fast jet is produced. This is indeed the case for the bubble close to the top of a rigid cylinder. The dynamics of the bubble in this case provoke the association with a mushroom shape. The present work investigates the details of the dynamics in the parameter range $0.047 < D^* < 2.009$ and $0.251 < r_p^* < 0.893$.

2. EXPERIMENTAL METHODS

The observation of the laser-induced bubble in the experiment is described briefly here. For a detailed explanation, the reader is referred to [1].

The bubble is produced in the center of a rectangular cuvette of edge length $1\,cm \times 5\,cm \times 4\,cm$ (width, depth, height), filled with de-ionized water. The laser for bubble seeding is an Nd:YAG Litron nano PIV, operated at $\lambda = 532\,nm$ with a single pulse duration of $10\,ns$. The laser light is fist widened and then focused into the center of the cuvette by a lens of $35\,mm$ focal distance.

For the rigid cylinder, a sewing needle was ground to flat top. The needle radius was measured to be $r_p = 272.8\,\mu m$.

Two cameras are applied for observing the bubble, each equipped with a long distance microscope objective (K2 Infinity). For Mega-frames per second recording of the collapse of the bubble the Imacon 468 was used (8 images in total) and for kiloframes per second recording of the overall dynamics the Photron APS-RX was used. The record trigger for the Imacon Camera has to be known with $1\,\mu s$ precision. This was accomplished with a continuous wave Helium-Neon laser that points onto a photodiode through the site of bubble generation.

Backlight illumination was done with a xenon-flash (*Mecablitz*).

3. BUBBLE MODEL AND NUMERICAL METHODS

The bubble model consists of two phases, one gas phase (air) and one liquid phase (water) that do not exchange mass. Viscosity of both phases is included, while surface tension and gravity are neglected in this case, as well as evaporation or condensation processes. The two phases are considered isentropic, which is valid up to shock waves of $\approx 3\,GPa$ [26, page 40]. Therefore, the energy equation for the set of momentum equations for the compressible phases can be omitted and can be substituted by two equations of state: the adiabatic gas equation and the Tait-equation

$$\text{gas: } \frac{p}{p_\infty} = \left(\frac{\rho}{\rho_n}\right)^{\gamma}, \quad \text{liquid: } \frac{p+B}{p_\infty + B} = \left(\frac{\rho}{\rho_\infty}\right)^{n_\mathrm{T}}, \tag{3}$$

where $\gamma = 1.4$ is the polytropic exponent of air, $\rho_n = 1.204\,kg/m^3$, $B = 305\,MPa$ a constant and $n_\mathrm{T} = 7.15$, the Tait-exponent.

The model is implemented in a finite volume solver running in the open source `foam-extend` software package for computational fluid dynamics. This solver is maintained and developed since 2013 (for an extended description, including validation, see e.g. [27, 28, 19, 23]).

The governing equations are the Navier-Stokes equation and the continuity equation

$$\frac{\partial(\rho \boldsymbol{U})}{\partial t} + \nabla \cdot (\rho \boldsymbol{U} \otimes \boldsymbol{U}) =$$
$$-\nabla p + \nabla \cdot \left[\mu\left(\nabla \boldsymbol{U} + (\nabla \boldsymbol{U})^T - \frac{2}{3}(\nabla \cdot \boldsymbol{U})\,\mathbb{I}\right)\right], \tag{4}$$

$$\frac{\partial \rho}{\partial t} + \nabla \cdot (\rho \boldsymbol{U}) = 0\,, \quad \frac{\partial \alpha_i \rho}{\partial t} + \nabla \cdot (\alpha_i \rho \boldsymbol{U}) = 0\,, \tag{5}$$

where $\boldsymbol{U}$ denotes the velocity, $\otimes$ the tensorial product, ∇ the gradient and $\nabla\cdot$ the divergence, μ the dynamic viscosity and $\mathbb{I}$ the unit tensor. The two phases are distinguished by a phase parameter $\alpha \in [0, 1]$ such that, e.g., $\mu = \alpha\mu_l + (1-\alpha)\mu_g$ with μ_l, μ_g the viscosities of the liquid and the gas respectively. The subscript i denotes either l (liquid) or g (gas), where $\alpha_l = \alpha$ and $\alpha_g = 1 - \alpha$.

The computational domain is discretized with the finite volume method and the equations are solved in a segregated manner by the PISO algorithm (pressure implicit with splitting of operators).

3.1. Initial data

The calculations have been performed mainly in axial symmetry. Distinct simulations in full 3D have been made for a qualitative comparison, as well. The size of the computational domain for the axisymmetric calculations was chosen to be $52\,mm$, while the maximum radii in unbounded liquid $R_{\text{max,unbound}}$ of the bubbles tested ranged from $224\,\mu m$ to $636\,\mu m$. At $t = 0$ the liquid is at rest and the bubble is compressed to $20\,\mu m$ in all of the 89 cases studied. The cells of the mesh are oriented in the radial direction, only the core of the mesh is in cartesian orientation. The cylinder with a radius of either $200\,\mu m$ or $160\,\mu m$ was cut out of the mesh. The boundary condition at the cylinder is set to no-slip and $\alpha = 1$ (= liquid). The outer boundary of the mesh is set to be wave transmissive. Details for the mesh are found in [1].

3.2. Hardware

The simulations in axial symmetry were done on a dual Xenon Silver 4216 machine with 32 cores and 93.1 *GB* RAM. Each simulation comprised about 125 000 cells and 30 000 time steps, consuming about 1h15min of computational time for $110\,\mu s$.

4. RESULTS

Before describing the results of the bubbles on top of a cylinder, the case for $l_\mathrm{p} = 0$ is recapitulated. In Figure 2 the pressure and velocity field of an axisymmetric simulation of a bubble at $D^* = 0.04$, $l_\mathrm{p} = 0$ are shown for six times shortly before minimum bubble volume in order to elucidate the different jetting mechanism. An annular jet forms on the top of the bubble. The liquid impacts onto itself before the bubble could involute like it would do for $D^* \geq 0.24$. Within a fraction of a microsecond a small part of the liquid is accelerated to, here, more than $1200\,m/s$. More information about this phenomenon is found in [18, 19, 23, 24, 1], as well as in the CMFF'22 article by C. Lechner.

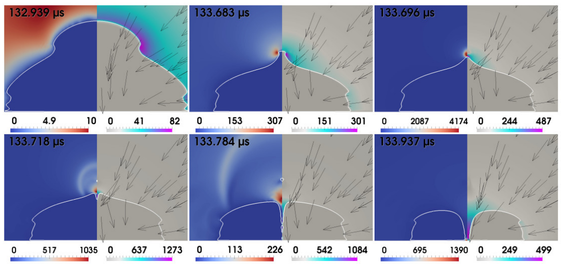

Figure 2. Simulation showing the fast-jet mechanism. Reprinted from [23, Fig. 5.1]. Left part of the frames: pressure field in bar, right part of the frames: velocity field in m/s.

Figure 3 shows the recording of a bubble at $D^* = 0$, $l_\mathrm{p} \gg r_\mathrm{p}$, $r^*_\mathrm{p} \approx 0.32$ with the photron camera. Radius of the cylinder top is $r_\mathrm{p} = 272.8\,\mu m$. Exposure time is $1\,\mu s$. The sequences of four recordings at 21 kfps each were stacked and interleaved. The times for one of the sequences are given and the frames without a time tag are from different sequences used for interpolation. The bubble has a maximum horizontal width of $1689\,\mu m \pm 18\,\mu m$ at $95.2\,\mu s$.

In order to classify the different parts of the shape of the bubble at different times, the terminology given in Figure 4 is applied. The dynamics of the bubble in Fig. 3 can now be described in the following way: At first, the bubble expands to a radius about 3 times larger than the cylinder radius. Before minimum volume during collapse, the lower part seems to form a waist and the bottom of the bubble forms the *bottom stand foot* (two frames before $190.5\,\mu s$). When the neck tapers (one frame before $190.5\,\mu s$), the mushroom cap of the bubble becomes even more evident. During bubble volume minimum ($190.5\,\mu s$), the shape becomes cloudy by

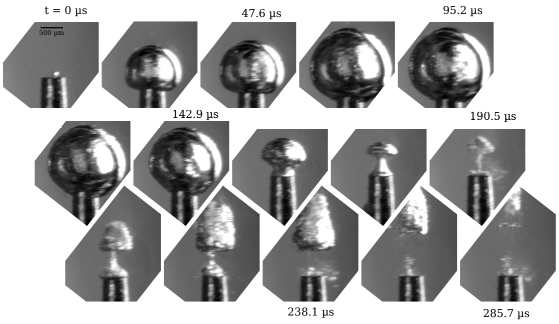

Figure 3. Image sequence of a typical mushroom bubble generated at $D^* \approx 0$, $l_p \gg r_p$, recorded with the photron camera. Reprinted from [1].

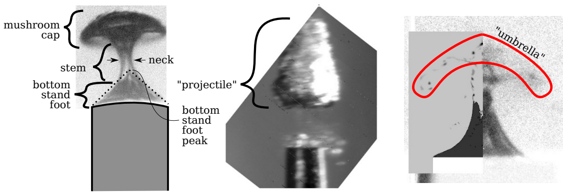

Figure 4. Terminology for mushroom-shaped bubbles. [1]

fragmentation into many small gas parts and subsequently the mushroom cap grows and detaches as a *projectile*.

In order to gain insight into why the mushroom shape of the bubble is formed and whether it is persistent to a wider range of the $[D^*, r^*_p]$ parameter space, 89 simulations in axial symmetry have been performed, out of which 68 showed the mushroom shape. 18 frames of one simulation with typical dynamics are shown in Figure 5 with arrows indicating the main flow. The color indicates the magnitude of the velocity of the liquid in m/s. The characteristic values of the bubble are: $R_{\text{max,unbound}} = 472.57\,\mu m$, $D^* = 0.063$, $r^*_p = 0.423$, $t_{Rc} = 42.90\,\mu s$. Cylinder radius is $200\,\mu m$. Frames 1–9 show the expansion and the begin of the collapse, while frames 10–18 show the moment of jetting with a *fast jet*, the bubble minimum volume and rebound with the detaching of the projectile.

During the expansion phase, shown in the first 3 frames the bubble interface crosses the cylinder rim, it swirls around it (frame 2), ejecting liquid droplets (in axial symmetry torus ring drops) into the bubble body. Once passed, these droplets hit the outer bubble wall, inducing surface waves there (dashed circles in frame 3). Due to the boundary layer around the cylinder, the bubble never touches the solid, but “swims” on the boundary layer. ([1]).

When the bubble starts collapsing, the outer waist is lifted almost parallel to the cylinder. This flow produces the two annular inflows that form a) a neck and b) the extreme curvatures at the mushroom cap rim. As denoted by the red arrows and circles in frame 7, Fig. 5, the flow that forms the mushroom neck has also a component upwards that tapers the cap to a thin gas film. The phenomenon of *flow focusing* comes into play [29, 19], flow focusing generating strongest acceleration where curvatures are highest. An annular jet is formed that runs along the top part of the shrinking mushroom cap, leaving trails of dim remnant gas that form a thin umbrella (see e.g. Fig. 4, right frame). Numerically, this results into a tearing of the interface, leaving areas where $0.9 < \alpha < 1$. In the end, this annular liquid jet impacts in the zenith of the umbrella, producing a *fast jet*. The fast jet actually is the reason, why the neck will not impact onto itself . It can be seen that the fast jet here reaches values of more than 700 *m/s* (see dashed rectangle on top of the velocity scale in frame 11). In some cases, it is more than 2000 *m/s*, as will be shown later. The liquid inflow from the top now, starting from frame 10 on, makes all sideways inflows at the neck negligible, changing the subsequent dynamics to a zipper-like collapse. The neck is tapered from inside rather than from outside flows. In the experiment, only the aforementioned “bottom stand foot” is observed here, because the outside bubble surface has too many wrinkles to see the jet inside. The minimum volume happens from top-down, thus the top gas fragments are already in the rebound phase, when the lower ones collapse and emit shock waves (not seen here – taking place in frame 16, as indicated by the dashed red circle in the frame). Therefore, the upper bubbles are “kicked” and squeezed upwards. Thereby, a layered structure of (torus) bubbles is observed. ([1]).

Experimental insight into the moment of mushroom bubble jetting can be gained with the Imacon camera. Figure 6 shows such a record of 8 frames at a time during ring jet impact at the top of the mushroom cap. The times denote the delay to the camera trigger. The background of the experimental images was subtracted. The recorded images are compared to a simulation via an overlay with the volume fraction field α on the left side of each frame (mind that the numerical simulation is represented by a cut through the bubble). The characteristic values for the bubble of the simulation are $D^* = 0.057$ and $r^*_p = 0.306$. The frame width for the experiment is $766\,\mu m \pm 10\,\mu m$. The cylinder radius r_p in the experiment is $272.8\,\mu m$, in the simulation r_p is $200\,\mu m$. It is seen that the simulation and the experiment match very well, even the torus-shaped mushroom cap rim is reproduced by the simulation. It is also evident from the simulation that the stem/neck of the bubble is pierced by the fast jet, producing the top-down zipper-like collapse that is also seen in the experiment. For more comparisons, 3D simulations and experimental recordings, the reader again is referred to [1].

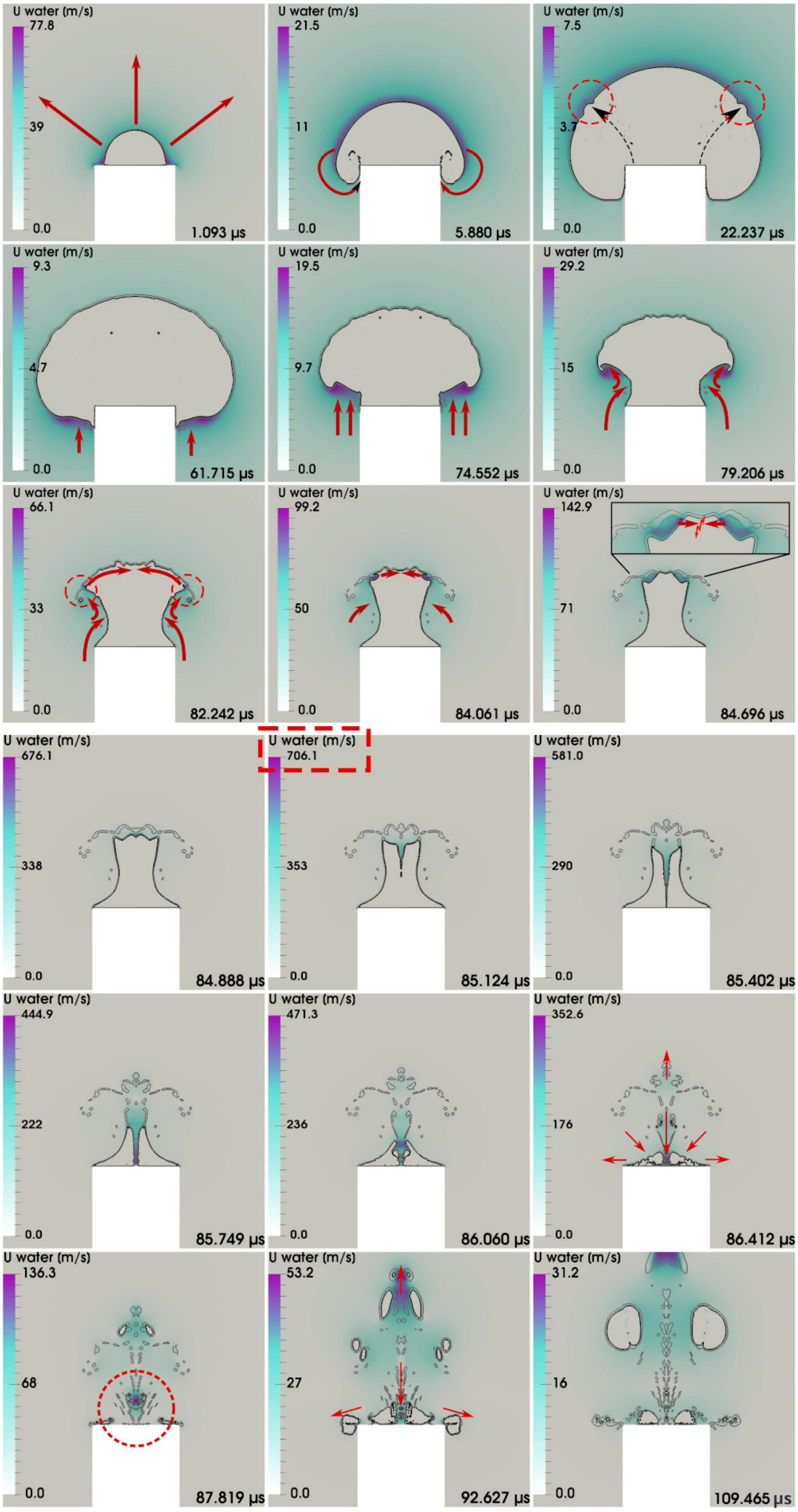

Figure 5. General dynamics of the mushroom bubble. [1]

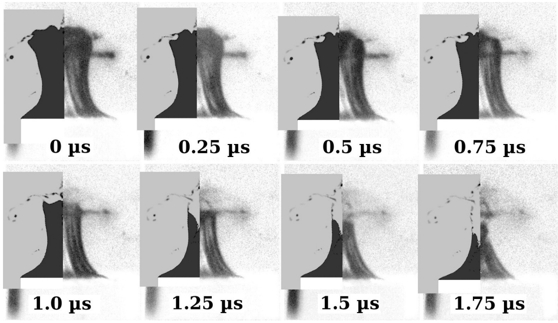

Figure 6. Imacon camera frame sequence of a mushroom bubble at a time during ring jet impact at the top of the mushroom cap. [1]

With the figures given in this manuscript, the main line of reasoning concerning the link between the mushroom shape and the fast jet is sketched.

4.1. Parameter study

The 89 simulations were evaluated and distinct quantities were extracted to be plotted into an interpolated heat map with isocurves within the $[D^*, r_p^*]$ parameter space. Two of the graphs from [1] are shown in Figure 7. Each data point represents one simulation. The data points are plotted in their respective colors that represent their values. White data points denote cases, where either the bubble dynamics was different from the mushroom case, the annular jet impact happens later than the neck closure or a standard jet by involution of the bubble wall was observed.

The jet speed (top graph) was calculated by the distance of the spot of the annular jet impact to the top of the cylinder divided by the time the liquid needs to traverse this distance. This speed, however, did not converge yet for any mesh and time resolution (see explanation in [19, 1]). Therefore, the values ranging from 189 m/s to 2164 m/s are given as tentative results. The corresponding water hammer pressures ($\rho\, c\, v_{\mathrm{jet}}$) would range from 0.3 GPa to 3 GPa. The heat map suggests that the faster jets are found for low values of r_p^* and higher values of D^*.

In the bottom graph the length of the jet is given, measured from the point of formation to the point of impact onto the pillar surface. When the jet length is compared to the cylinder radius , the jet becomes longer for smaller r_p^* as well (for a fixed r_p). The jet length varied by less than 10 % with grid alterations. It could be an interesting quantity from an experimental point of view, when photographing the jet is planned. ([1]).

5. FURTHER STUDIES

In addition to the material from [1] a glimpse into a probable reason for erosion, first assessed in [23], is given here. For the case of $l_p = 0$ the pressure signal in the symmetry point below the bubble at the solid wall, gained by an axisymmetric simulation, was compared to the dynamics of the bubble:

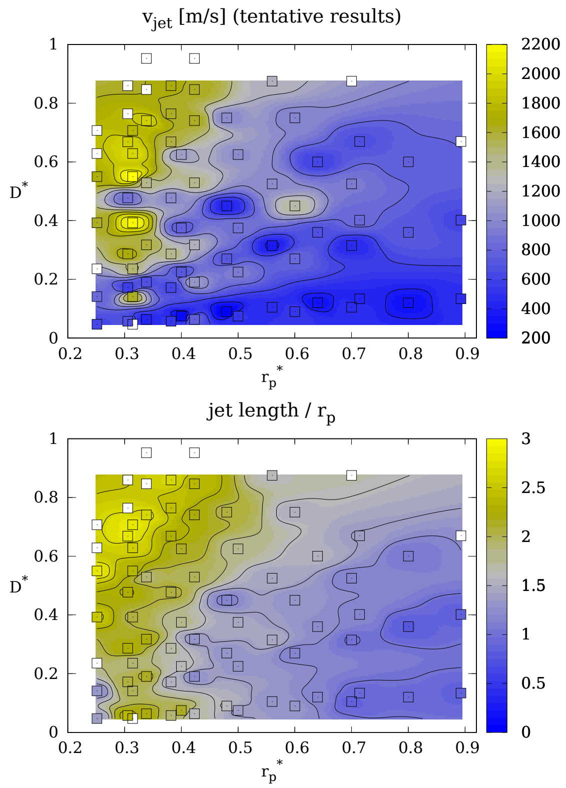

Figure 7. Part of the parameter study (see [1]). Reprinted with different colors.

It is most likely that the main erosion (for $l_p = 0$) happens around $D^* = 0.1$, where peak values of close to 4 GPa are observed. A first evaluation for the reason of this pressure peak is given in Figure 8 for $D^* = 0.1$. Shown is the bubble with the pressure field in bar during and after fast jet impact, as well as the aforementioned pressure signal. The fast jet has already impacted onto the solid boundary before the main pressure peak at 111.65 μs. The main peak roots from the focusing of the toroidal shockwave from the collapse of the bubble directly on the solid boundary. From this simulation, it can be said that one single, laser generated bubble of $R_{\max} \approx 500\,\mu m$ might be able to erode an alloy when generated at a distance of $D^* = 0.1$. ([23]). Detailed experimental studies on erosion tests have been performed by [30, 31].

6. SUMMARY

A laser-induced bubble on top of a long cylinder with a radius at maximum volume larger than the radius of the cylinder shows a dynamics very different from a bubble on an extended flat surface. After having embraced the cylinder top upon expansion, upon collapse it develops a mushroom shape with a head, a long stem and a footing. The special fluid flow leading to the mushroom shape could be reproduced in numerical studies by solving the Navier-Stokes equations for a Tait-compressible liquid with OpenFOAM (precisely the foam-extend fork). The

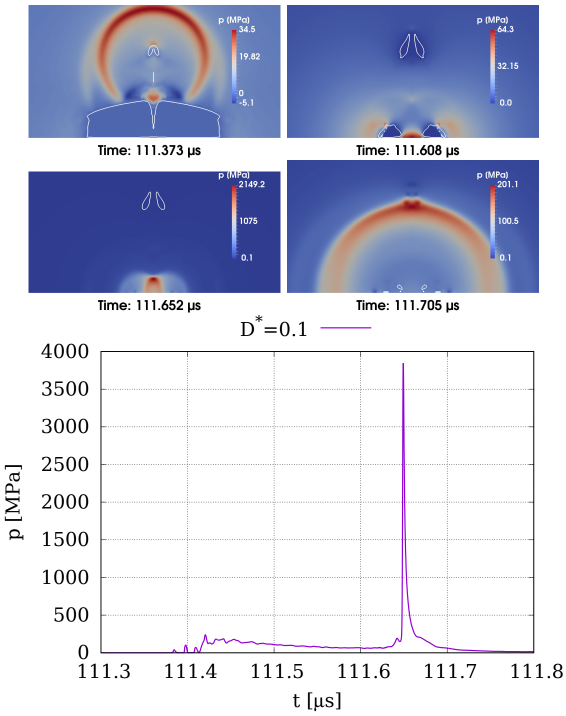

Figure 8. Towards shock waves as reason for erosion. [23]. Top four frames: pressure field [bar] around a bubble at $D^* = 0.04$, $l_p = 0$ at times of fast jet formation and minimum volume. Bottom Frame: Pressure signal [MPa] in the symmetry point below the bubble at the solid boundary showing the large pressure peak from the focusing of the torus shock wave, generated at torus-bubble collapse on the surface.

simulations were carried out in axial symmetry . The simulation code has been validated again by comparison of an experimental with a numerical mushroom shape (Fig. 6). A quite large range of parameters has been studied ($0.047 \leq D^* \leq 2.009$ and $0.251 \leq r_p^* \leq 0.893$). In 68 of 89 cases investigated, the bubble forms a mushroom shape and the mushroom head collapses with forming a fast jet (velocity ranging from 189 m/s to 2164 m/s) into the gaseous stem from the self-impact of an annular inflow by two-dimensional flow focusing. The existence of the fast jet in the experiments has been proven by comparing the experiments with the numerical simulations with respect to stem stability. The range of parameters shows that fast jets of annular-inflow type (studied numerically in [18, 21, 19] and experimentally in [23, 24] for bubbles close to a plane solid boundary) are not a singular phenomenon, but a robust phenomenon. It is expected to occur in many other configurations, too, and to alter the view on cleaning and erosion of surfaces. It may find applications in laser-induced ablation in liquids with pillars of various shapes as targets for laser synthesis and processing of colloids [32]. The fast jet phenomenon also bears a clear potential for erosion of solids. ([1]).

The indication that another cause for erosion might stem from the toroidal shockwave of the bubble collapse has been shown as well for one data point in the parameter subset.

ACKNOWLEDGEMENTS

The work was supported in part by the German Science Foundation (DFG) under contracts ME 1645/8-1, ME 1645/8-3 and ME 1645/5-2 and the Austrian Science Fund (FWF) (Grant No. I 5349-N).

References

[1] M. Koch, J. M. Rosselló, C. Lechner, W. Lauterborn and R. Mettin. “Dynamics of a laser-induced bubble above the flat top of a solid cylinder — mushroom-shaped bubbles and the fast jet”. In: *Fluids* 7.1 (2022).

[2] M. Kauer, V. Belova-Magri, C. Cairós, G. Linka and R. Mettin. “High-speed imaging of ultrasound driven Cavitation bubbles in blind and through holes”. In: *Ultrason. Sonochem.* 48 (2018), pp. 39–50.

[3] B. Karri, K. S. Pillai, E. Klaseboer, S.-W. Ohl and B. C. Khoo. “Collapsing bubble induced pumping in a viscous fluid”. In: *Sensors and Actuators A: Physical* 169.1 (2011), pp. 151–163.

[4] T. Trummler, S. H. Bryngelson, K. Schmidmayer, S. J. Schmidt, T. Colonius and N. A. Adams. “Near-surface dynamics of a gas bubble collapsing above a crevice”. In: *J. Fluid Mech.* 899 (July 2020), A16-1–21.

[5] E. D. Andrews, D. F. Rivas and I. R. Peters. “Cavity collapse near slot geometries”. In: *J. Fluid Mech.* 901 (Sept. 2020), A29-1–22.

[6] Y. Tomita, P. B. Robinson and R. P. Tong. “Growth and collpase of cavitation bubbles near a curved rigid boundary”. In: *J. Fluid Mech.* 466 (2002), pp. 259–283.

[7] E. W. Quah, B. Karri, S.-W. Ohl, E. Klaseboer and B. C. Khoo. “Expansion and collapse of an initially off-centered bubble within a narrow gap and the effect of a free surface”. In: *International Journal of Multiphase Flow* 99 (2018), pp. 62–72.

[8] S. R. Gonzalez-Avila, A. C. van Blokland, Q. Zheng and C.-D. Ohl. “Jetting and shear stress enhancement from cavitation bubbles collapsing in a narrow gap”. In: *J. Fluid Mech.* 884 (2020), A23-1 –A32-23.

[9] S. Li, A.-M. Zhang, R. Han and Q. Ma. “3D full coupling model for strong interaction between a pulsating bubble and a movable sphere”. In: *J. Comput. Phys.* 392 (Sept. 2019), pp. 713–731.

[10] J. Zevnik and M. Dular. "Cavitation bubble interaction with a rigid spherical particle on a microscale". In: *Ultrasonics Sonochemistry* 69 (2020), p. 105252.

[11] D. Palanker, A. Vankov, J. Miller, M. Friedman and M. Strauss. "Prevention of tissue damage by water jet during cavitation". In: *J. Appl. Phys.* 94.4 (Aug. 2003), pp. 2654–2661.

[12] D. Kim and D. Kim. "Underwater bubble collapse on a ridge-patterned structure". In: *Phys. Fluids* 32.5 (May 2020), p. 053312.

[13] E. Kadivar, O. el Moctar, R. Skoda and U. Löschner. "Experimental study of the control of cavitation-induced erosion created by collapse of single bubbles using a micro structured riblet". In: *Wear* 486-487 (2021), p. 204087.

[14] Y. Zhang, X. Qiu, X. Zhang, N. Tang and Y. Zhang. "Collapsing dynamics of a laser-induced cavitation bubble near the edge of a rigid wall". In: *Ultrason. Sonochem.* 67 (Oct. 2020), p. 105157.

[15] M. Senegačnik, K. Kunimoto, S. Yamaguchi, K. Kimura, T. Sakka and P. Gregorčič. "Dynamics of laser-induced cavitation bubble during expansion over sharp-edge geometry submerged in liquid – an inside view by diffuse illumination". In: *Ultrason. Sonochem.* 73 (May 2021), p. 105460.

[16] Q. Wang, M. Mahmud, J. Cui, W. R. Smith and A. D. Walmsley. "Numerical investigation of bubble dynamics at a corner". In: *Phys. Fluids* 32.5 (May 2020), p. 053306.

[17] W. Lauterborn, C. Lechner, M. Koch and R. Mettin. "Bubble models and real bubbles: Rayleigh and energy-deposit cases in a Tait-compressible liquid". In: *IMA J. Appl. Math.* 83 (2018), pp. 556–589.

[18] C. Lechner, W. Lauterborn, M. Koch and R. Mettin. "Fast, thin jets from bubbles expanding and collapsing in extreme vicinity to a solid boundary: A numerical study". In: *Phys. Rev. Fluids* 4 (2 Feb. 2019), p. 021601.

[19] C. Lechner, W. Lauterborn, M. Koch and R. Mettin. "Jet formation from bubbles near a solid boundary in a compressible liquid: Numerical study of distance dependence". In: *Phys. Rev. Fluids* 5.9 (Sept. 2020), p. 093604.

[20] O. V. Voinov and V. V. Voinov. "On the process of collapse of a cavitation bubble near a wall and the formation of a cumulative jet". In: *Sov. Phys. Dokl.* 21 (1976), pp. 133–135.

[21] Y. A. Pishchalnikov, W. M. Behnke-Parks, K. Schmidmayer, K. Maeda, T. Colonius, T. W. Kenny and D. J. Laser. "High-speed video microscopy and numerical modeling of bubble dynamics near a surface of urinary stone". In: *J. Acoust. Soc. Am.* 146 (2019), pp. 516–531.

[22] T. B. Benjamin and A. T. Ellis. "The Collapse of Cavitation Bubbles and the Pressures thereby Produced against Solid Boundaries". In: *Philos. Trans. R. Soc. London, Ser. A* 260 (1966), pp. 221–240.

[23] M. Koch. "Laser cavitation bubbles at objects: Merging numerical and experimental methods". http://hdl.handle.net/21.11130/00-1735-0000-0005-1516-B. PhD thesis. Georg-August-Universität Göttingen, Third Physical Institute, 2020.

[24] M. Koch, J. M. Rosselló, C. Lechner, W. Lauterborn, J. Eisener and R. Mettin. "Theory-assisted optical ray tracing to extract cavitation-bubble shapes from experiment". In: *Exp. Fluids* 62.3 (Mar. 2021), p. 60.

[25] F. Reuter and C.-D. Ohl. "Supersonic needle-jet generation with single cavitation bubbles". In: *Appl. Phys. Lett.* 118.134103 (2021).

[26] R. H. Cole. *Underwater explosions*. Princeton, New Jersey: Princeton University Press, 1948.

[27] M. Koch. "Numerical modelling of cavitation bubbles with the finite volume method". English. https://doi.org/10.25625/JVCJVW. Master thesis. Georg-August Universität Göttingen, Drittes Physikalisches Institut, C. D. Labor für Kavitation und Mikro-Erosion, 2014.

[28] M. Koch, C. Lechner, F. Reuter, K. Köhler, R. Mettin and W. Lauterborn. "Numerical modeling of laser generated cavitation bubbles with the finite volume and volume of fluid method, using OpenFOAM". In: *Comput. Fluids* 126 (2016), pp. 71–90.

[29] W. Lauterborn. "Cavitation bubble dynamics — new tools for an intricate problem". In: *Appl. Sci. Res.* 38.1 (1982), pp. 165–178.

[30] A. Philipp and W. Lauterborn. "Cavitation erosion by single laser-produced bubbles". In: *J. Fluid Mech.* 361 (1998), pp. 75–116.

[31] M. Dular, T. Požar, J. Zevnik and R. Petkovšek. "High speed observation of damage created by a collapse of a single cavitation bubble". In: *Wear* 418-419 (2019), pp. 13–23.

[32] D. Zhang, B. Gökce and S. Barcikowski. "Laser synthesis and processing of colloids: fundamentals and applications". In: *Chem. Rev.* 117.5 (Feb. 2017), pp. 3990–4103.